crystals

MDPI

Article

Experimental Investigation of Phase Equilibria in the Ti—Al—Zr System at 1000–1300 °C

Zahra Kahrobaee [1,*], Boryana Rashkova [2], Katja Hauschildt [3] and Martin Palm [1]

[1] Max-Planck-Institut für Eisenforschung GmbH (MPIE), Max-Planck-Straße 1, 40237 Düsseldorf, Germany
[2] Department of Physical Metallurgy and Materials Testing, Montanuniversität Leoben, Roseggerstr. 12, A-8700 Leoben, Austria
[3] Institute of Materials Physics, Helmholtz-Zentrum Hereon, 21502 Geesthacht, Germany
* Correspondence: z.kahrobaee@mpie.de

Abstract: Four partial isothermal sections of the Ti—Al—Zr system up to 60 at. % Al and 30 at. % Zr were experimentally established between 1000–1300 °C. Six heat-treated alloys were analysed by scanning electron microscopy, transmission electron microscopy, electron probe microanalysis, conventional and high-energy X-ray diffraction, and differential thermal analysis. Phase equilibria were determined between B2-ordered (β_0), βTi,Zr, αTi, Ti_3Al, TiAl, and $ZrAl_2$.

Keywords: phase diagram; phase transitions; microstructure; crystal structures

Citation: Kahrobaee, Z.; Rashkova, B.; Hauschildt, K.; Palm, M. Experimental Investigation of Phase Equilibria in the Ti—Al—Zr System at 1000–1300 °C. *Crystals* **2022**, *12*, 1184. https://doi.org/10.3390/cryst12091184

Academic Editors: Jun Tan and Quan Dong

Received: 30 July 2022
Accepted: 18 August 2022
Published: 23 August 2022

Publisher's Note: MDPI stays neutral with regard to jurisdictional claims in published maps and institutional affiliations.

1. Introduction

After more than thirty years of development, TiAl-based alloys were employed as low-pressure turbine (LPT) blades in aero engines in 2006 [1]. By the application of TiAl-based alloys, which replaced much heavier Ni-based superalloys, CO_2 and NO_x emissions and noises produced by aircrafts could be successfully reduced [1]. Up to 1000 °C, TiAl-based alloys show higher specific yield strength than Ni-based superalloys [2]. However, due to their limited creep and oxidation resistance, their application is currently limited to temperatures below 800 °C, and therefore, TiAl-based alloys have to be further developed to fully realize their potential in improving the efficiency of aero-engines [3].

The addition of Zr improves the creep resistance of TiAl-based alloys by decreasing the c/a ratio of the phase TiAl, thereby reducing the misfit between TiAl and Ti_3Al in the lamellar microstructure and thus retarding coarsening of the lamellae at high temperatures [4–6]. In addition, solid solution hardening of TiAl increases strength at all temperatures [7], and therefore, Zr was introduced in the newly developed TNM AM alloy (TNM refers to a class of TiAl-based (T) alloys strengthened by Nb (N) and Mo (M), here Ti-43.5Al-4Nb-1Mo-0.1 B at. % adopted for additive manufacturing (AM)) [8]. Additionally, Zr is a β-stabilizing alloying element in Ti-alloys [9], and in Ti—Al alloys containing higher amounts of Zr, B2-ordered β_0 has been observed [10–13]. Although the composition and temperature range where β_0 exists has not been established, the ductility of TiAl-based alloys deteriorates if β_0 transforms to the brittle hexagonal ω_0-phase at lower temperatures [14–18].

Thus, the addition of Zr is of high interest in the development of advanced TiAl-based alloys. In order to substantially reduce the time for new alloy developments, CALPHAD (CALculation of PHAse Diagram) is currently widely used to predict phase equilibria, phase transitions, solidification paths and other thermodynamic information important for the optimization of compositions, the processing and design of heat-treatments of novel alloys. As CALPHAD predicts phase equilibria of higher-order systems based on extrapolation of data from the binary and ternary systems, the reliability of the modelling crucially depends on the underlying database, which is extracted from experimental investigations from the constituent binary and ternary systems [19].

In a first step, a complete assessment of all available literature on phase equilibria in the Ti—Al—Zr system was performed [20]. From this assessment, it is clear that discrepancies exist, especially between recent CALPHAD modellings [21,22] and experimentally determined phase equilibria [6,11,23–25]. As pointed out in the assessment [20] as well as in the modellings [21,22], specifically at 800 °C, even the multi-phase equilibria are not settled, e.g., the experiments show TiAl in equilibrium with βTi at 800 °C, while the CALPHAD modellings show equilibria between TiAl and Zr_4Al_3 [21] or between TiAl and $ZrAl_2$ [22], which "cut off" any possible phase equilibrium between TiAl and βTi. In consequence, adjacent phase equilibria differ completely from each other within a wide composition range at 800 °C in [20–22]. Furthermore, at higher temperatures, experimental results and modelling are at variance, specifically regarding the extension of the various binary phases into the ternary system, and little is known about the stability of β_0. The discrepancies arise from the lack of reliable experimental data, resulting from practical difficulties in establishing phase equilibria in the Ti—Al—Zr system, such as the high susceptibility of Zr to oxygen uptake and its often-poor purity, which both can significantly influence the phase equilibria [20]. Therefore, the assessment and the modelling came to the conclusion that new reliable experimental data in the Ti—Al—Zr system are needed to resolve these issues [20,21].

The present work is performed within the large-scale European project ADVANCE to set up the next generation of advanced CALPHAD databases for Ti—Al—X(—Y) systems, which are relevant for developing TiAl-based alloys with improved properties [26]. As a part of this project, phase equilibria in the Ti—Al—Zr system were experimentally investigated focusing on the temperature range 1000–1300 °C, to assist in the development of TiAl-based alloys for even higher application temperatures and in the temperature range, where the alloys are thermally processed to attain specific microstructures. Crystallographic data of all phases observed in the present investigation are listed in Table 1. However, other phases have been reported within the investigated composition range [20].

Table 1. Crystallographic data of solid phases.

Phase, Temperature Range (°C)	Space Group; Strukturbericht Designation	Lattice Parameters (nm)
βTi,Zr, <1855–863	$Im\bar{3}m$; A2	a_0 = 0.33065 for pure Ti [27] a_0 = 0.36090 for pure Zr [28] a_0 = 0.3228 at 35.1 at. % Ti, 23.7 at. % Al, 41.2 at. % Zr [24]
αTi, 1491–1120 and <1170	$P6_3/mmc$; A3	a_0 = 0.29506; c_0 = 0.46835 [27]
Ti_3Al (α_2), <1200	$P6_3/mmc$; $D0_{19}$	a_0 = 0.5765; c_0 = 0.4625 [29] a_0 = 0.5783; c_0 = 0.4667 at 52.1 at. % Ti, 28.0 at. % Al, 19.9 at. % Zr [24]
TiAl (γ), <1456	$P4/mmm$; $L1_0$	a_0 = 0.4000; c_0 = 0.4075 at 50 at. % Al [30] a_0 = 0.4080; c_0 = 0.4087 at ~42 at. % Ti, ~47 at. % Al, ~11 at. % Zr [31] a_0 = 0.3974; c_0 = 0.4072 at 41.5 at. % Ti, 50.6 at. % Al, 7.9 at. % Zr [24]
Zr_5Al_3, <1400–1000	$I4/mcm$; $D8_m$	a_0 = 1.1044; c_0 = 0.5391 [28]
Zr_5Al_3, (<1000?)	$P6_3/mcm$; $D8_8$	a_0 = 0.8174; c_0 = 0.5698 [28] a_0 = 0.8217; c_0 = 0.5704 at 30.5 at. % Ti, 39.2 at. % Al, 30.3 at. % Zr [24]
$ZrAl_2$, <1624	$P6_3/mmc$; C14	a_0 = 0.52824; c_0 = 0.87482 [28] a_0 = 0.5273; c_0 = 0.8827 at 8.7 at. % Ti, 60.1 at. % Al, 31.2 at. % Zr [24]
β_0	$Pm\bar{3}m$; B2	a_0 = 0.333(6) at 50 at. % Ti, 25 at. % Al, 25 at. % Zr [11]

2. Materials and Methods

From elements of high purity (Ti: 99.995%; Al: 99.999%; Zr: 99.95%; HMW Hauner, Röttenbach, Germany), six alloys were prepared by crucible-free levitation melting (Fives Celes) [32]. Thus, any reactions between melt and crucible are avoided, yielding alloys of high purity. Rods of 15 mm in diameter and 150 mm in length were produced by casting into a cold copper mould. Compositions of the alloys and their impurity contents were determined by wet-chemical analysis, employing inert gas fusion (NCS Fusion Master ONH) for oxygen and nitrogen, combustion gas analysis (NCS Combustion Master CS) for carbon, and inductively coupled plasma optical emission spectroscopy (PerkinElmer Optima 8300 ICP-OES, Waltham, MA, USA) for all other elements.

For heat treatments at 1000 and 1100 °C, slices of the alloys were encapsulated in high-purity quartz capsules back-filled with Ar. Ti filings were used as getter, separated from the sample to avoid contact between the getter and the sample. Heat treatments at temperatures above 1100 °C, where quartz capsules are no longer gas tight [33], were performed under flowing dry Ar using a double-crucible technique [32,34]. After annealing at 1300 and 1200 °C for 24 h, 1100 °C for 200 h, and 1000 °C for 100 or 1000 h, all samples were quenched to room temperature (RT). After heat treatment, wet-chemical analyses were performed on selected samples to check the impurity uptake, which revealed only small increases in the oxygen content (Table 2). Comparison of the overall compositions of the as-cast alloys and after heat treatment also revealed that no preferential evaporation of Al occurred even at 1300 °C (Table 2).

Scanning electron microscopy (SEM; Zeiss, LEO 1550 VP, Oberkochen, Germany) was used to study the microstructures. Phases were identified in the quenched samples by X-ray diffraction (XRD; Bruker, Advance D8, Billerica, MA, USA) at RT on powders with a particle size <90 µm. Using Co-Kα (λ = 0.178897 nm) radiation, measurements were carried out in the 2-Theta range of 20° to 120° in Bragg–Brentano geometry. XRD spectra were analysed with the X'Pert HighScore software (PANalytical, Malvern, UK), and phases were identified with the Powder Diffraction File TM (PDF2; International Centre for Diffraction Data ICDD) [35]. Lattice parameters were calculated using TOPAS (Bruker AXS-Version 5).

Transmission electron microscopy (TEM) was applied at Montanuniversität Leoben using a Philips CM12 operated at 120 kV. The chemical compositions of the phases were determined by energy-dispersive X-ray spectroscopy (EDXS) from EDAX. TEM lamellae were prepared by ion milling carried out in a focused ion beam (FIB; Versa 3D FEI Thermofisher, Waltham, MA, USA). The techniques are described in [36,37].

High-energy XRD (HE-XRD) was used to characterize phases in some samples in addition to XRD, specifically in cases of low-phase fractions. HE-XRD experiments were conducted at the High-Energy Materials Science (HEMS) beam-line [38,39] at the synchrotron storage ring PETRA III at DESY Hamburg, Germany, operated by Hereon. The measurements were performed with a photon energy of 100 keV (λ = 0.0124 nm) and a beam size of 0.5 × 0.5 mm^2. The samples with a thickness of 2 mm were measured in transmission. For each measurement, the samples were rotated during the exposure time by 120° to acquire better grain statistics. The diffraction patterns were recorded with a 2D flat panel detector (PerkinElmer XRD 1621). Subsequently, the data were integrated over 360° azimuthal angle using the program Fit2d [40].

Compositions of the coexisting phases were measured by electron probe microanalysis (EPMA; JEOL, JXA-8100, Akishima, Japan) on metallographic sections. Qualitative analyses were performed at 15 kV, 400 nA with a beam width of 3 µm to check for the presence of any impurities. For quantitative analysis, pure elements were utilized as standards. Quantitative analyses were performed at 15 kV, 20 nA with a focused beam. A minimum of 12 measurements for each phase were performed at least at five different places of the samples. Analyses were discarded if the total mass of Ti + Al + Zr was not in the range of 99 to 101 mass %. Final compositions were achieved through ZAF matrix correction.

For the determination of phase transformation temperatures, differential thermal analysis (DTA; NETZSCH, STA 449 F3 Jupiter, Selb, Germany) was performed under a stream of pure Ar, using alumina crucibles. Samples annealed at 1000 °C were heated up to a maximum of 1450 °C and cooled down to RT at 10 K/min for two times. Although all heating/cooling cycles were analysed, reported transformation temperatures are onset temperatures evaluated from the first heating cycle. By calibration through the melting points of pure Al, Au and Ni, the experimental uncertainty was established to be ±1 K.

3. Results and Discussion

Four partial isothermal sections at 1000–1300 °C have been established. The overall compositions of alloys in as-cast and heat-treated states are summarized in Table 2. Wet-chemical analysis of slices taken from the different parts of the as-cast alloy Z5 proved that

this alloy is homogeneous. Comparison of wet-chemical analyses of various heat-treated samples with the overall composition of the as-cast alloys indicates that these are also homogeneous, with the exception of Z4, where the difference in the Zr content between analyses of the as-cast and the two heat-treated samples hints to some inhomogeneity within this specific alloy.

Table 2. Wet-chemical analyses of the as-cast alloys and after various heat treatments.

Alloy	Condition	Ti (at. %)	Al (at. %)	Zr (at. %)	C wt. % ppm	O wt. % ppm	N wt. % ppm
Z1	as-cast	69.3	20.6	10.1	110	350	<50
Z2	as-cast	63.2	27.4	9.4	160	370	<50
	1000 °C/ 100 h	61.8	28.4	9.8	147	510	<50
Z4	as-cast	44.0	40.8	15.2	137	340	<50
	1000 °C/ 100 h	38.3	44.7	16.5	111	455	<50
	1300 °C/ 24 h	40.6	43.3	16.1	89	300	<50
Z5 *	as-cast	48.8 ± 0.2	46.1 ± 0.3	5.1 ± 0.01	127 ± 10	110 ± 30	<50
	1000°C/ 100 h	48.8	46.1	5.1	100	200	<50
Z6	as-cast	44.7	45.1	10.2	120	400	<50
	1300 °C/ 24 h	45.1	44.6	10.3	89	480	<50
Z7	as-cast	37.0	47.3	15.7	79	180	<50
	1300 °C/ 24 h	38.1	46.6	15.3	77	240	<50

* Average of two measurements from slices cut from the top and bottom of the alloy rod.

Data for the binary systems are taken from the following references: Al—Zr from the assessment by Schuster [28], which is in agreement with all other recent assessments and thermodynamic modellings; Ti—Zr from the latest available assessment by Malfliet et al. [41], and Ti—Al from Palm [42]. For a detailed discussion on the selected, binaries see [20]. Compared to [20], the Ti—Al system is taken from a more recent update of the original assessment [43]. In the updated assessment, particularly the possibility of B2-ordering in βTi is discussed. Additionally, it shows that the previous difference between experiments and modelling for phase equilibria between αTi, βTi and Ti_3Al can be settled when vacancies and anti-site defects are included in the modelling.

3.1. Partial Isothermal Section at 1000 °C

Figure 1 depicts the partial isothermal section at 1000 °C. The compositions of coexisting phases and their lattice parameters are presented in Table 3.

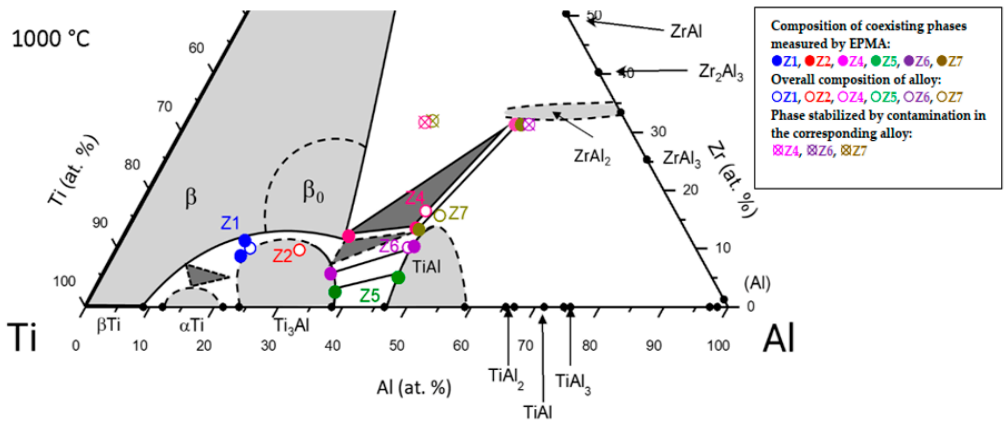

Figure 1. Partial Ti—Al—Zr isothermal section at 1000 °C.

Table 3. Compositions and lattice parameters of the coexisting phases and impurity contents of samples annealed at 1000 °C. Data for HT represent the duration of heat-treatments; data shown in *italics* are from HE-XRD; phases marked with an asterisk (*) formed during quenching.

Alloy	HT (h)	Composition				Lattice Parameters (nm)			Impurity (wt. ppm)		
		Phases	Ti (at. %)	Al (at. %)	Zr (at. %)	Phases	a_0	c_0	C	O	N
Z1	1000	βTi, Zr or β_0	69.5 ± 0.2	19.1 ± 0.3	11.4 ± 0.2	αTi *	0.29420 (1) *0.2952*	0.47307 (3) *0.472*			
		Ti_3Al	71.4 ± 0.3	19.8 ± 0.3	8.8 ± 0.2	Ti_3Al	0.58982 (2) *0.5878*	0.46911 (2) *0.4707*			
Z2	100	Ti_3Al	63.2 ± 0.6	27.4 ± 0.2	9.4 ± 0.5	Ti_3Al	0.58700 (7)	0.46979 (5)	147	510	<50
		$ZrAl_2$	17.5 ± 0.7	51.3 ± 0.4	31.2 ± 0.4	$ZrAl_2$	0.53756 (1) *0.537*	0.87478 (3) *0.8745*			
Z4	100	TiAl	41.8 ± 0.3	44.7 ± 0.2	13.5 ± 0.3	TiAl	0.40963 (2) *0.411*	0.40976 (4) *0.408*	111	455	<50
		β_0	53.0 ± 0.3	34.9 ± 0.2	12.1 ± 0.2	β_0	0.327 (1) *0.3268*				
Z5	100	TiAl	48.7 ± 0.4	46.2 ± 0.3	5.1 ± 0.3	TiAl	0.40453 (4)	0.40900 (7)	100	200	<50
		Ti_3Al	59.9	37.5	2.6	Ti_3Al	0.5813 (4)	0.4651 (6)			
Z6	1000	TiAl	43.6 ± 0.9	46.0 ± 0.5	10.4 ± 0.5	TiAl	0.40737 (4)	0.41061 (6)			
		Ti_3Al	59.0 ± 0.3	35.3 ± 0.3	5.7 ± 0.1	Ti_3Al	0.5825 (2)	0.4666 (3)			
Z7	1000	$ZrAl_2$	16.5 ± 0.4	52.2 ± 0.6	31.3 ± 0.3	$ZrAl_2$	0.53688 (2)	0.87237 (5)			
		TiAl	41.7 ± 0.7	45.1 ± 0.5	13.2 ± 0.3	TiAl	0.40942 (2)	0.40955 (2)			

Initial heat treatments at 1000 °C were performed for 100 h. Although samples were in equilibrium after 100 h, grains of individual phases were somewhat small for EPMA. Therefore, the annealing time was increased to 1000 h in subsequent heat treatments. Alloy Z4 shows the three-phase equilibrium β_0 + TiAl + $ZrAl_2$, as established by EPMA, (HE-) XRD (Figure 2) and TEM. TEM selected-area diffraction patterns confirm (Figure 3) that the Zr-rich phase is the hexagonal Laves phase $ZrAl_2$, in agreement with the results by XRD and HE-XRD. The TEM investigations also show that $ZrAl_2$, which contains 17.5 at. % Ti, is still the C14-type Laves phase, i.e., the same polymorph as binary $ZrAl_2$. The existence of the equilibrium β_0 + TiAl + $ZrAl_2$ rules out that TiAl is in equilibrium with Zr_5Al_3 at this temperature [24]. However, Zr_5Al_3 is also observed in a small amount in Z4, but in contrast to the other three phases, it always contains about 2% mass of impurities, mostly oxygen. The HE-XRD spectrum in Figure 2 shows that Z4 contains only a minor amount of Zr_5Al_3. By HE-XRD, the structure of Zr_5Al_3 was identified as hexagonal $P6_3/mcm$ ($D8_8$, Mn_5Si_3-type). In contrast to Zr_5Al_3 of the tetragonal W_5Si_3-type, the Mn_5Si_3-type is only observed for Zr_5Al_3 when oxygen occupies otherwise empty octahedral sites in this structure [44]. Therefore, this phase is considered to show up when stabilized by impurities, as already observed in other systems [45,46]. Phase equilibria between TiAl and adjacent phases have also been studied at 1000 °C by Tanda et al. [47]. For alloys with nominal composition of 45, 50, and 55 at. % Al and 20 at. % Zr as well as for 60 at. % Al and 25 at. % Zr, they observed TiAl in equilibrium with $ZrAl_2$. This is in agreement with the present investigation (Figure 1). Additionally, it supports that Zr_5Al_3 is only observed within this composition range if it is stabilized by oxygen.

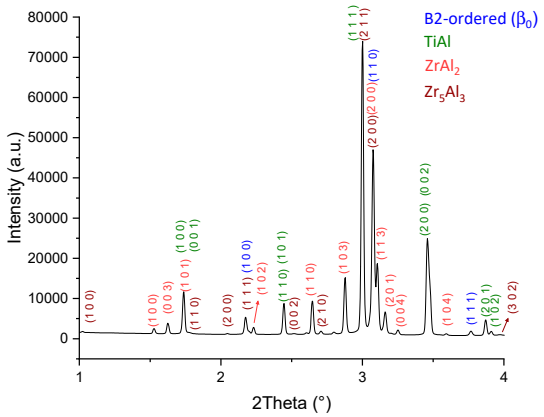

Figure 2. HE-XRD analysis of Z4 (Ti-44.7Al-16.5Zr at. %) heat treated at 1000 °C/100 h.

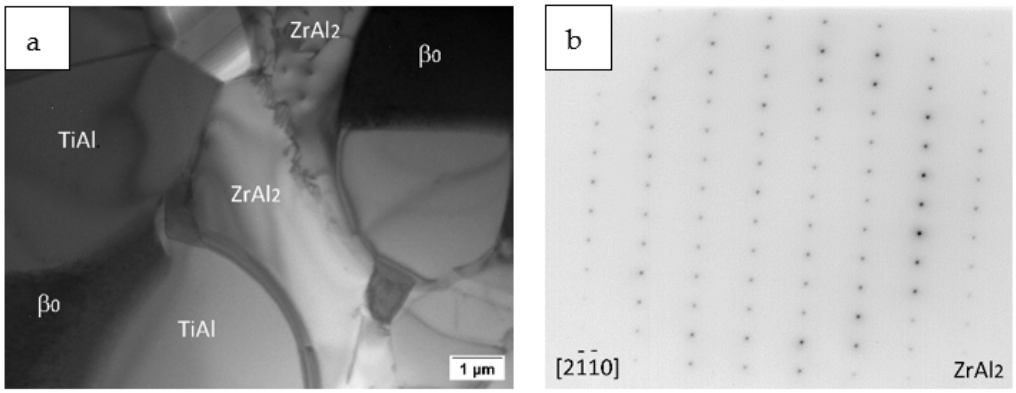

Figure 3. Z4 (Ti-44.7Al-16.5Zr at. %), heat treated at 1000 °C/1000 h; (**a**) TEM bright field, (**b**) diffraction pattern of $ZrAl_2$.

The TEM investigations also show that B2-ordered β_0 is present in Z4 at 1000 °C. Analysis of the anti-phase boundaries (APBs) showed only the presence of a few thermal APBs. If β_0 would have formed by ordering from disordered βTi,Zr during quenching, this would have yielded a large amount of APBs. Correspondingly B2-ordered β_0 is stable at 1000 °C.

The SEM micrograph of Z1 in Figure 4a shows a two-phase microstructure of Ti_3Al + βTi,Zr or β_0, where the needle- or lath-shaped contrast in the latter phase indicates transformation during quenching. The TEM bright-field image (Figure 4b) reveals the presence of martensite, which is typical for the transformation from βTi to αTi [48,49]. Because of this martensitic transformation, it is no longer possible to ascertain whether disordered βTi,Zr or β_0 was present at 1000 °C. The formation of the martensite explains why αTi is observed at RT in Z1 (Table 3).

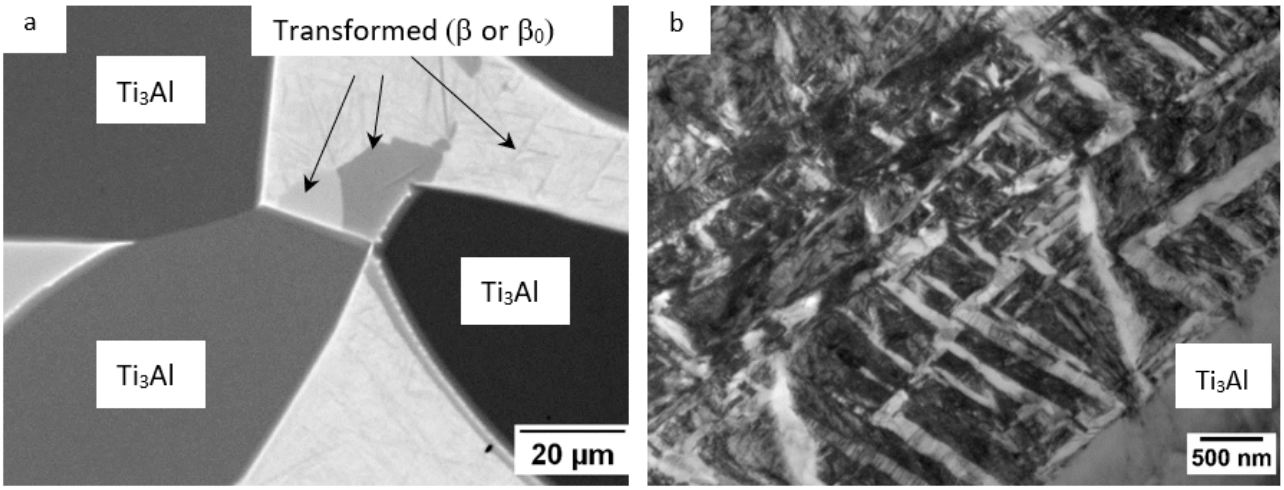

Figure 4. Microstructure of Z1 (Ti-20.6Al-10.1Zr at. %), heat treated at 1000 °C/1000 h: (**a**) SEM back-scattered electron (BSE) micrograph, (**b**) TEM bright field (BF) micrograph.

Compared to the assessed data [20], Zr shows a significantly larger solid solubility in TiAl at 1000 °C. The solid solubility of Zr in TiAl was given with 8.5 at. % in the assessment [20], in agreement with [24]. According to Figure 1, the solid solubility of Zr in TiAl is actually about 13.5 at. % at 1000 °C, in satisfactory agreement with about 11 at. % in [31] and 15 at. % in [47]. Data in [24] are for TiAl in equilibrium with Zr_5Al_3 and are therefore presumably much lower than otherwise observed. For the solid solubility of Zr in Ti_3Al, data in the assessment [20] are also based on [24], where a solid solubility of nearly 20 at. % Zr has been measured. The present data show that the solid solubility is

only about 10 at. % Zr in Ti_3Al at 1000 °C. Again, this discrepancy is attributed to the fact that the much higher solid solubility in [24] is found for Ti_3Al in equilibrium with Zr_5Al_3.

Complete isothermal sections at 1000 °C in [21,22], which are calculated based on the data in [6,24], matched qualitatively with the assessed data in [20]. However, as detailed above, the newly established phase equilibria in Figure 1 differ from those in [20,24]. Therefore, the CALPHAD modellings in [21,22] show different multiple phase equilibria than the ones established here. Consequently, it is possible that solid solubilities of the third element in the binary phases such as βTi,Zr, Ti_3Al, and $ZrAl_2$ deviate notably in the modellings from those established here.

3.2. Partial Isothermal Section at 1100 °C

The partial isothermal section at 1100 °C is shown in Figure 5; the compositions of coexisting phases and their lattice parameters are presented in Table 4. In addition, in alloys heat treated at 1100 °C, Zr_5Al_3 was sometimes observed (Figure 6). In those cases, EPMA measurements were performed far away from this phase for minimalizing its influence on the compositions. Phase equilibria are similar to those at 1000 °C. In contrast to the partial isothermal section at 1000 °C, alloys Z1 and Z2 locate in the single-phase field of βTi,Zr/β_0 and were therefore not heat treated at temperatures above 1000 °C. That these two alloys do not undergo phase transformations at higher temperatures is confirmed by DTA (see below).

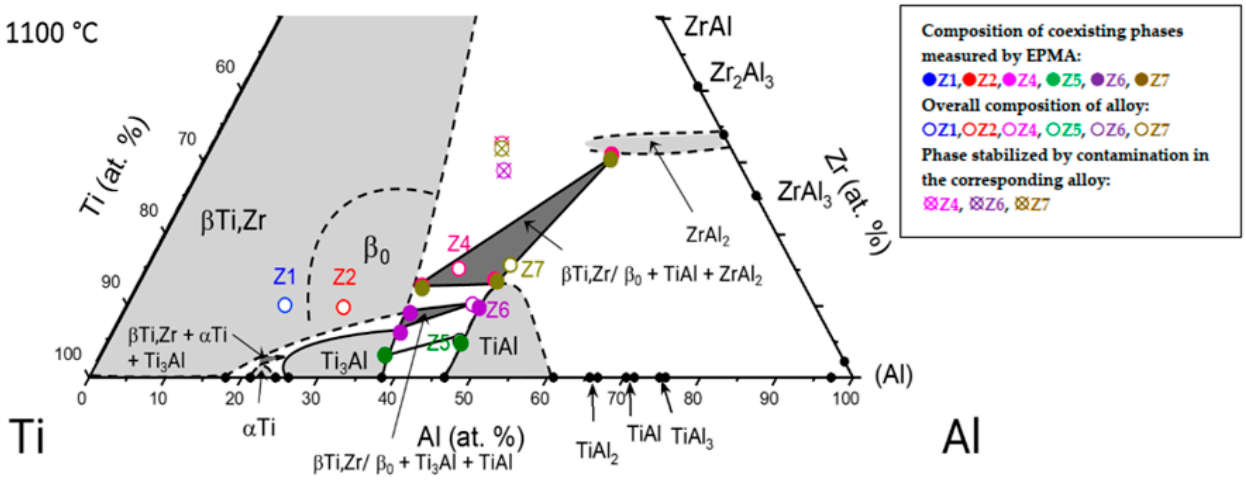

Figure 5. Partial Ti—Al—Zr isothermal section at 1100 °C.

Table 4. Compositions and lattice parameters of the coexisting phases in alloys heat treated at 1100 °C/200 h; n.d.: not determined, but phase is detected.

Alloy	Composition				Lattice Parameters (nm)		
	Phases	Ti (at. %)	Al (at. %)	Zr (at. %)	Phases	a_0	c_0
Z4	$ZrAl_2$	16.0 ± 0.6	52.9 ± 0.3	31.1 ± 0.5	$ZrAl_2$	0.53461 (1)	0.87451 (2)
	TiAl	40.0 ± 0.6	46.3 ± 0.2	13.7 ± 0.5	TiAl	0.4095 (1)	0.4115 (4)
	β_0	50.0 ± 0.5	37.2 ± 0.3	12.8 ± 0.3	β_0	0.322 (8)	
Z5	TiAl	48.9 ± 0.9	46.3 ± 0.6	4.8 ± 0.3	TiAl	0.40443 (3)	0.40845 (5)
	Ti_3Al	59.7 ± 0.6	37.2 ± 0.5	3.1 ± 0.1	Ti_3Al	0.5798 (1)	0.4665 (2)
Z6	TiAl	43.5 ± 0.2	46.8 ± 0.2	9.7 ± 0.2	TiAl	0.40716 (4)	0.41024 (6)
	Ti_3Al	56.1 ± 0.3	37.6 ± 0.2	6.3 ± 0.1	Ti_3Al	0.5822 (2)	0.4680 (3)
	β (or β_0)	53.5 ± 0.3	37.5 ± 0.1	9.0 ± 0.2	β (or β_0)	n.d.	
Z7	$ZrAl_2$	16.5 ± 0.3	53.1 ± 0.3	30.4 ± 0.3	$ZrAl_2$	0.53771 (1)	0.87419 (3)
	TiAl	39.9 ± 0.4	46.7 ± 0.4	13.4 ± 0.2	TiAl	0.41051 (2)	0.41094 (2)
	β_0	50.1 ± 0.5	37.4 ± 0.4	12.5 ± 0.2	β_0	0.327 (1)	

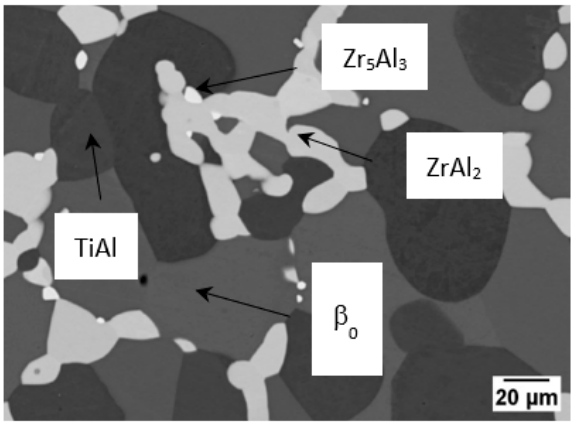

Figure 6. BSE micrograph of alloy Z4 (Ti-40.8Al-15.2Zr at. %) heat treated at 1100 °C/200 h showing the phase equilibrium β_0 + $ZrAl_2$ + TiAl and sporadic small grains of Zr_5Al_3.

At 1100 °C, alloys Z4 and Z7 comprise β_0 + TiAl + $ZrAl_2$, and alloy Z6 represents the three-phase equilibrium β_0 + Ti_3Al + TiAl. From the overall composition of Z6, it is evident that the sample contains only a minor volume fraction of β_0. Therefore, it was not possible to establish the ordering by XRD, but from the results at 1000 °C (Figure 1) and 1200 °C (Figure 7), and the DTA investigation of Z6 (see below), it may be concluded that the phase is B2-ordered β_0 in Z6 at 1100 °C.

Data from the literature for 1100 °C are scarce, and most of them stem from the 1960s, where a series of vertical sections starting from the Ti corner has been established from metallography, DTA and XRD [25,50–54]. As discussed in detail in [20], most of the results are questionable, and they are therefore not considered. The most relevant data stem from an investigation of the homogeneity range of TiAl at 1093 °C [55] (original reference unavailable, but data are shown and discussed in [56]). The maximum solid solubility of Zr in TiAl was found to be about 9 at. % at 1093 °C; however, the equilibrium for which this solid solubility was found is not given in [55]. In the present investigation, the highest Zr content in TiAl is about 13.5 at. %, observed for the equilibrium β_0 + TiAl + $ZrAl_2$ in alloys Z4 and Z7 (Table 4). For the drawing of the dashed βTi,Zr/β_0 phase boundary in Figure 5, the result by Jiang et al. [57] has been considered, who found βTi,Zr to be present in Ti-15Al-40Zr at. % solution treated at 1100 °C/2 h.

3.3. Partial Isothermal Section at 1200 °C

The partial isothermal section at 1200 °C is shown in Figure 7, and compositions of coexisting phases, lattice parameters, and analysed impurity contents are presented in Table 5.

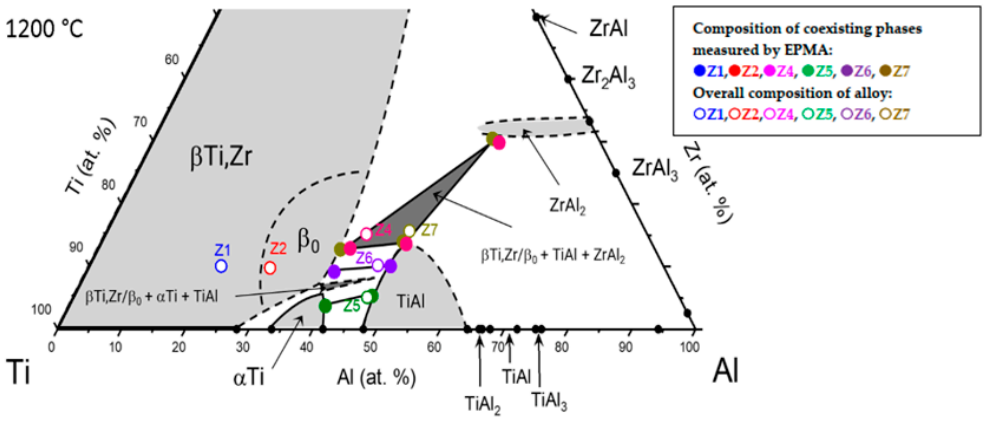

Figure 7. Partial Ti—Al—Zr isothermal section of the at 1200.

Table 5. Compositions and lattice parameters of the coexisting phases and impurity contents of samples heat treated at 1200 °C/24 h; data shown in italics are from HE-XRD; phases marked with an asterisk (*) ordered during quenching.

Alloy	Composition				Lattice Parameters (nm)			Impurity (wt. ppm)		
	Phases	Ti (at. %)	Al (at. %)	Zr (at. %)	Phases	a_0	c_0	C	O	N
Z4	$ZrAl_2$	15.9 ± 0.4	54.3 ± 0.5	29.8 ± 0.2	$ZrAl_2$	0.53439 (1)	0.87378 (2)	140	250	<50
	TiAl	38.5 ± 0.3	47.9 ± 0.3	13.6 ± 0.1	TiAl	0.40916 (7)	0.4119 (1)			
	β_0	47.7 ± 0.7	39.4 ± 0.6	12.9 ± 0.3	β_0	0.327 (1)				
Z5	TiAl	48.0 ± 0.3	46.7 ± 0.3	5.3 ± 0.2	TiAl	0.40459 (5) *0.4049*	0.40867 (8) *0.4072*	120	240	<50
	αTi	56.1 ± 0.4	40.1 ± 0.4	3.8 ± 0.1	αTi	0.2900 (1)	0.4646 (4)			
					Ti_3Al *	*0.579*	*0.4638*			
Z6	TiAl	42.7 ± 0.5	47.2 ± 0.7	10.1 ± 0.4	TiAl	0.40397 (4) *0.4078*	0.40868 (7) *0.4085*	110	770	<50
	β_0	52.0 ± 0.7	38.8 ± 0.8	9.2 ± 0.3	β_0	0.338 (2) *0.3253*				
Z7	$ZrAl_2$	16.6 ± 0.3	53.0 ± 0.4	30.4 ± 0.3	$ZrAl_2$	0.53614 (5) *0.5357*	0.8742 (2) *0.873*	100	360	<50
	TiAl	38.9 ± 0.6	47.1 ± 0.5	14.0 ± 0.2	TiAl	0.40908 (3) *0.410*	0.41162 (5) *0.4095*			
	β_0	49.3 ± 0.3	37.9 ± 0.3	12.8 ± 0.2	β_0	0.326 (5) *0.32665*				

Comparison with data for the as-cast alloys (Table 2) reveals that all samples show only a moderate uptake of oxygen after heat treatment at 1200 °C, with the exception of Z6. Compared to the partial isothermal section at 1100 °C, Ti_3Al is no longer present at this temperature, and the three-phase equilibrium β_0 + αTi + TiAl is now observed. The reaction observed by DTA at about 1185 °C in Z5 should therefore stem from the reaction αTi + TiAl <−> Ti_3Al + TiAl. However, Ti_3Al was detected by HE-XRD in Z5 at RT after quenching from 1200 °C, showing once more that ordering from αTi to Ti_3Al took place during cooling. The presence of β_0 in alloys Z4, Z6 and Z7 is shown by XRD and HE-XRD.

The phase boundary between βTi,Zr and β_0 in Figure 7 is again shown by a dashed line, as it has not yet been established. However, in the drawing, it is considered that Ti-24.8Al-24.9Zr (at. %) was found to be single-phase B2-ordered β_0 by TEM after solution treating at 1200 °C for 30 min followed by water quenching [11] and that in a diffusion study, disordered βTi,Zr was found up to about 20 at. % Al and 39 at. % Zr at 1200 °C [58]. In addition, a large number of alloys was annealed at 1200 °C in the βTi,Zr/β_0 phase field by Kornilov and Boriskina [52] and Nartova and Shirokova [50]. Unfortunately, most of them underwent martensitic transformation during quenching, and therefore, no information about the ordering at 1200 °C can be gained from these samples.

None of the investigated alloys locate within the narrow tie triangle β_0 + αTi + TiAl at 1200 °C, which must be positioned in between the tie lines determined for Z5 and Z6. However, this composition range has been studied in detail by Kainuma et al. [6]. Comparison of their results with the present ones in Figure 8 shows an excellent match. Therefore, the position of the dashed three-phase field β_0 + αTi + TiAl in Figure 7 is taken from [6], slightly adjusted to agree with the binary Ti–Al system accepted here, which differs from the one accepted in [6]. It is noted that in [6], the authors did not distinguish between βTi,Zr and β_0, because no structural characterization by, e.g., XRD or TEM, was performed.

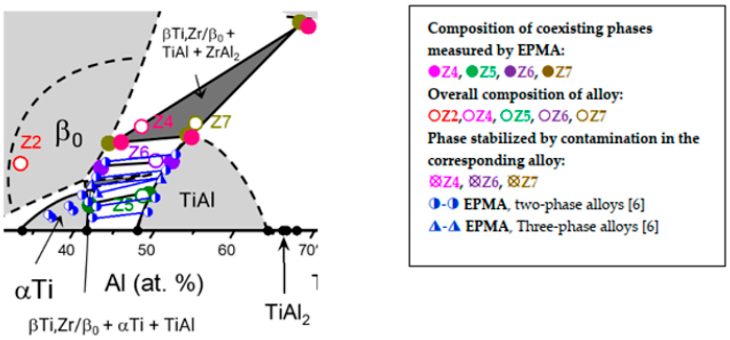

Figure 8. Enlarged section of the Ti—Al—Zr partial isothermal section at 1200 °C (Figure 7) with added EPMA data by [6].

Partial isothermal sections for compositions Ti-(30–60)Al-30Zr at. % Zr were calculated at 1200 °C in [21,22]. Although both modellings are based on data in [6], comparison of experimental data and modelling in [21,22] show an unsatisfactory match. Both modellings differ from phase equilibria shown in Figure 7, in that they show βTi,Zr in equilibrium with Zr_5Al_3 above about 15 at. % Zr. In contrast, the three-phase equilibrium of β_0 + TiAl + $ZrAl_2$ is observed in this study.

3.4. Partial Isothermal Section at 1300 °C

For the partial isothermal section at 1300 °C, compositions of the coexisting phases measured by EPMA and their lattice parameters are tabulated in Table 6. The partial isothermal section at 1300 °C based on these data is presented in Figure 9. In order to check whether preferential evaporation of Al occurred at this high temperature, the overall compositions of alloys Z4, Z6 and Z7 were analysed after the heat treatment at 1300 °C. The results are presented in Table 2 Concluding, if at all, only a small loss of Al is observed. Measurements of the impurities show that only the oxygen content slightly increased (Table 6).

Table 6. Compositions and lattice parameters of the coexisting phases in alloys heat treated at 1300 °C/24 h; n.d.: not determined, but phase is detected.

Alloy	Composition				Lattice Parameters (nm)			Impurity (wt. ppm)		
	Phases	Ti (at. %)	Al (at. %)	Zr (at. %)	Phases	a_0	c_0	C	O	N
Z4	$ZrAl_2$	15.9 ± 0.3	54.8 ± 0.3	29.3 ± 0.2	$ZrAl_2$	0.53530 (1)	0.87245 (3)	89	300	<50
	β_0	46.8 ± 0.4	41.0 ± 0.2	12.2 ± 0.3	β_0	0.326 (1)				
	TiAl	n.d.	n.d.	n.d.	TiAl	n.d.	n.d.			
Z5	TiAl	45.1 ± 0.4	49.2 ± 0.3	5.7 ± 0.2	TiAl	0.40383 (3)	0.40858 (4)	86	220	<50
	αTi	53.6 ± 0.8	42.4 ± 0.6	4.0 ± 0.2	αTi	0.28931 (4)	0.4639 (1)			
Z6	TiAl	41.2 ± 0.3	48.4 ± 0.3	10.4 ± 0.2	TiAl	0.40689 (3)	0.41080 (5)	89	480	<50
	β_0 (or β)	51.6 ± 0.9	39.3 ± 0.7	9.1 ± 0.3	β (or β_0)	0.325 (3)				
Z7	$ZrAl_2$	16.2 ± 0.4	54.1 ± 0.6	29.7 ± 0.4	$ZrAl_2$	0.53430 (1)	0.87287 (3)	77	240	<50
	TiAl	37.7 ± 0.3	48.6 ± 0.4	13.7 ± 0.3	TiAl	0.40852 (2)	0.41081 (2)			
	β_0	48.7 ± 0.9	38.9 ± 0.9	12.4 ± 0.2	β_0	0.325 (1)				

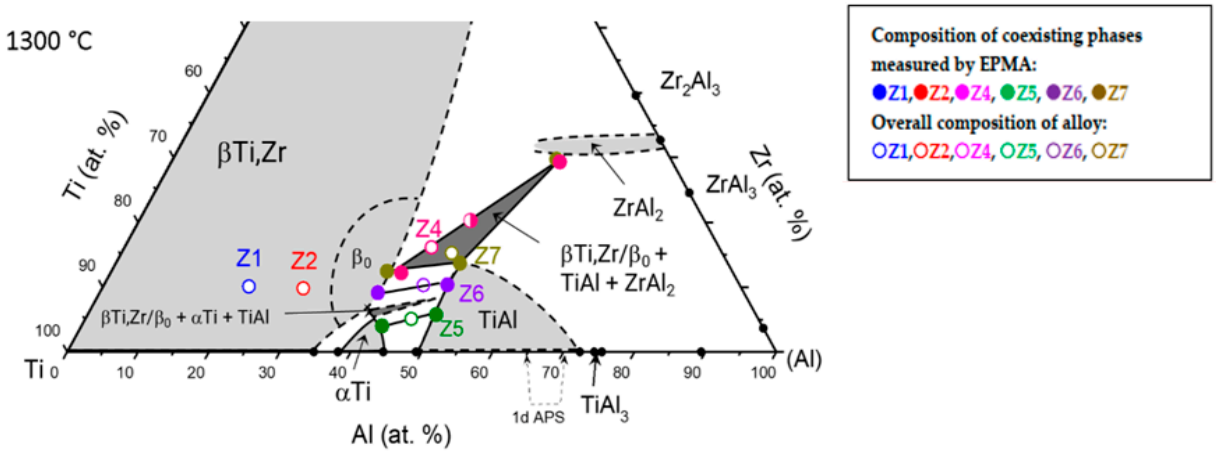

Figure 9. The partial Ti—Al—Zr isothermal section at 1300 °C.

Phase equilibria at 1300 °C resemble those at 1200 °C (Figure 7). The three-phase equilibrium β_0 + TiAl + $ZrAl_2$ is again observed in alloys Z4 and Z7. However, in the Z4, TiAl was only detected by XRD (Figure 10). Because of the minor phase fraction of TiAl, all grains were too small to be measured by EPMA. Alloys Z4 and Z7 show superlattice

reflections of β_0, while they are not visible for Z6. This could be due to the low phase fraction of β_0 in Z6, and therefore, the ordering cannot be established.

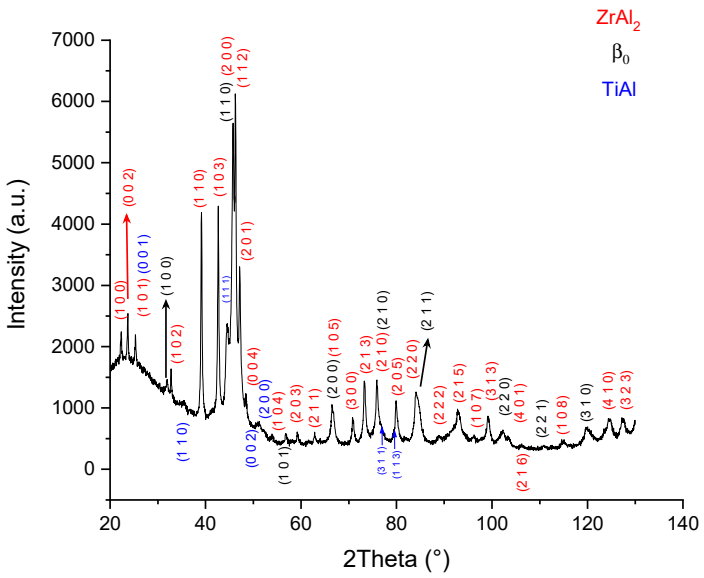

Figure 10. XRD analysis of Z4 (Ti-43.3Al-16.1Zr at. %) heat treated at 1300 °C/24 h.

Kainuma et al. [6] investigated phase equilibria among βTi,Zr(β_0), αTi, and TiAl at 1300 °C. They located the position of the narrow βTi,Zr(β_0) + αTi + TiAl three-phase field based on the established compositions of the neighbouring two-phase fields. Figure 11 shows that compositions determined in [6] agree with the current results. The small dashed tie triangles β_0 + αTi + TiAl in Figures 9 and 11 are derived from the combined results shown in Figure 11.

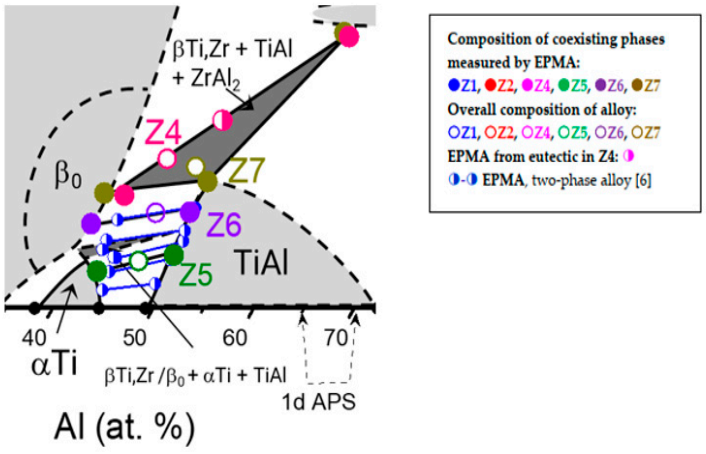

Figure 11. Enlarged section of the Ti—Al—Zr partial isothermal section at 1300 °C (Figure 9) with added EPMA data by [6].

The solid solubility range of TiAl at 1274 °C was investigated by metallography and XRD of quenched samples [56,59]. The data by Troup [56] actually stemmed from samples annealed between 1246 to 1379 °C, and therefore, he gave a range for the maximum solid solubility of 10 to 15 at. % Zr. Spragins et al. [59] found a maximum solid solubility of 13 at. % Zr at 1274 °C, although it was not stated at which equilibrium. As they detected oxides in some of their samples, and phase boundaries do not match with the accepted binary Ti—Al system, their values are considered as doubtful [20]. Furthermore, 13.7 at. % Zr have been measured in TiAl in Z7 (Table 6), but the solid solubility should be somewhat increased to higher Al contents.

In addition, for 1300 °C partial isothermal sections for the composition range Ti-(30–60)Al-30Zr at. % Zr were calculated in [21,22], based on data in [6]. Similarly, at 1200 °C, there is again no good match between the experimental data in [6]. Again, both modellings show phase equilibria between βTi,Zr(β_0) + Zr_5Al_3 instead of β_0 + TiAl + $ZrAl_2$ determined here.

In a small area near the outer edge, a eutectic is observed in alloy Z4 (Figure 12), indicating partial melting at 1300 °C. The composition of the eutectic measured with EPMA by employing a widened beam is Ti-46.8Al-20.3Zr at. %. A comparison with the recently established liquidus projection of the Ti—Al—Zr system by Abreu et al. [60] shows that the composition of the eutectic lies on the monovariant line L <–> βTi,Zr + $ZrAl_2$. While no temperatures are given in [60], DTA analysis of alloy Z4 shows that the eutectic temperature is 1316 ± 2 °C (Table 7 and Figure 12).

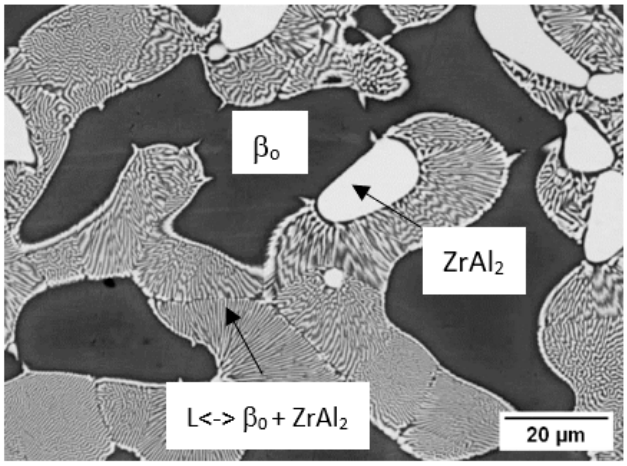

Figure 12. Microstructure at the outer edge of alloy Z4 (Ti-43.3Al-16.1Zr at. %) heat treated at 1300 °C/24 h.

3.5. DTA Analysis—Phase Transformation Temperatures

DTA was performed with samples equilibrated at 1000 °C. Table 7 summarizes the determined temperatures, allocation to certain reactions, and references for invariant reactions. Temperatures given in Table 7 are evaluated from the first heating, if not noted otherwise, and reactions are listed in the sequence of decreasing temperature.

Table 7. DTA results; reactions are shown and listed with decreasing temperature; strength of the peaks is indicated by ss (very strong), s (strong), and w (weak). As the ordering of βTi,Zr is not known when it precipitates from the melt, it is shown as βTi,Zr, although it might eb B2-ordered β_0.

Alloy	Al (at. %)	Zr (at. %)	Heated to °C	Onset (°C); Strength of the Peak	Reaction	Ref.
Z1	20.6	10.1	1400	1028; ss	βTi,Zr/β_0 <–> Ti_3Al + βTi,Zr/β_0	
				995; s	Ti_3Al + βTi,Zr/β_0 <–> Ti_3Al	
Z2	28.4	9.8	1400	1083 (±3); ss	β(Ti,Zr)/β_0 <–> Ti_3Al	
				1316; ss	L <–> βTi,Zr + $ZrAl_2$	[60]
Z4	44.7	16.5	1400	1235; s	?	
				890; s	?	
				850; s	?	
Z5	46.1	5.1	1400	~1185; w	αTi + TiAl <–> Ti_3Al + TiAl	
				1353; ss	L <–> L + βTi,Zr	[60]
Z6	45.1	10.2	1400	1314; s	L <–> TiAl + βTi,Zr	[60]
				~1190; w	β_0 + TiAl <–> β_0 + TiAl + Ti_3Al	
				1367; ss	L <–> βTi,Zr + $ZrAl_2$	[60]
Z7	47.3	15.7	1400	1312; ss	L <–> TiAl + βTi,Zr	[60]
				1219; s	?	

The peaks in alloy Z1 at 1028 and 995 °C are related to the transition from βTi,Zr (or β_0) to Ti_3Al. This would be in full agreement that the alloy Z1 consists of βTi,Zr (or β_0) + Ti_3Al at 1000 °C (Figure 1, Table 3) and locates in the single-phase field of βTi,Zr/β_0 at 1100 °C (Figure 5) and in the single-phase field of Ti_3Al at 800 °C [23]. A comparison of the isothermal sections at 1000 °C (Figure 1) and 1100 °C (Figure 5) shows that the strong peak observed for alloy Z2 at 1083 °C should also be related to the βTi,Zr/β_0 to Ti_3Al transition. That instead of two individual peaks only one peak is observed is in accordance with Figure 1, which shows that the βTi,Zr/β_0 + Ti_3Al two-phase field should be narrow in that composition range.

The peak at 1316 °C in alloy Z4 is associated with the eutectic L <−> βTi,Zr + $ZrAl_2$, as detailed above and in agreement with the liquidus projection [60]. The three peaks at 1219, 890, and 850 °C, were observed during first heating, and they cannot be allocated to any phase transformation. According to the present results, alloy Z4 consists of βTi,Zr/β_0 + TiAl + $ZrAl_2$ between 1300 and 1000 °C and at 800 °C according to [23]. Therefore, no peak is expected below 1300 °C in this alloy. The weak peak in alloy Z5 at 1185 °C should be associated with the transition from αTi + TiAl to Ti_3Al + TiAl, which is observed in Z5 between 1200 °C (Figure 7) and 1100 °C (Figure 5). The DTA curve of Z6, shows two distinct peaks above 1300 °C, which are related to the solidification of Z6. According to the liquidus projection [60], the composition of Z6 locates in the field of primary crystallization of βTi,Zr. Therefore, the peak at 1353 °C should correspond to the reaction L <−> L + βTi,Zr. Due to precipitation of βTi,Zr, the composition of the melt enriches in Al, shifting its composition towards the eutectic line L <−> βTi,Zr + TiAl [60]. The strong sharp peak at 1314 °C could therefore correspond to this reaction. The weak peak at about 1190 °C may be associated with the transition from the two-phase field β_0 + TiAl at 1200 °C (Figure 7) to the three-phase field β_0 + TiAl + Ti_3Al at 1100 °C (Figure 5). Again, the DTA of Z7 shows two distinct peaks above 1300 °C (Table 7). As the composition of Z7 is also located in the field of primary crystallization of βTi,Zr [60], the peak at 1367 °C should correspond to L <−> L + βTi,Zr. The peak at 1312 °C could correspond to L <−> βTi,Zr + $ZrAl_2$ according to [60], as the Zr content is markedly higher than in alloy Z6 and more comparable to that of alloy Z4 (Table 2). It is noted that eutectic temperatures determined in alloys Z4, Z6, and Z7 are close to each other. As they should stem from two different eutectic lines and as the composition of the ternary eutectic E_1 L <−> βTi,Zr + TiAl + $ZrAl_2$ in [60], where these two lines meet, must be close by, the temperature of E_1 could be at about 1310 °C. For Z7, there is one more peak at 1219 °C, which is only observed on the first heating; it cannot be allocated to any reaction, as Z7 consists of βTi,Zr + TiAl + $ZrAl_2$ between 1300 and 1100 °C (Figures 5 and 9).

3.6. Effect of Addition of Zr on the Lattice Parameters of TiAl

Because it has already been realised in the 1950s that the c/a ratio of TiAl decreases with increasing Zr content, much effort has been spent on this topic] [4,31,47,55,61,62] (for completeness: in some of the early studies, an increase in the c/a ratio with increasing Zr content was reported [56,59,63]. As reported data nearly approached unity, it had been expected that a possibly cubic structure could be attained for TiAl by alloying with Zr. Potentially, this could reduce the brittleness of TiAl. In view of the importance of this topic, the current c/a ratios are shown in Figure 13. The data once more reveal that the c/a ratio of TiAl markedly decreases depending on the increasing Zr content, but it does not reach or even exceed a value of 1. As also shown before] [31,47,60], the addition of Zr in TiAl does not change the c/a ratio monotonically. Additionally, the c/a ratio changes depending on the Al content.

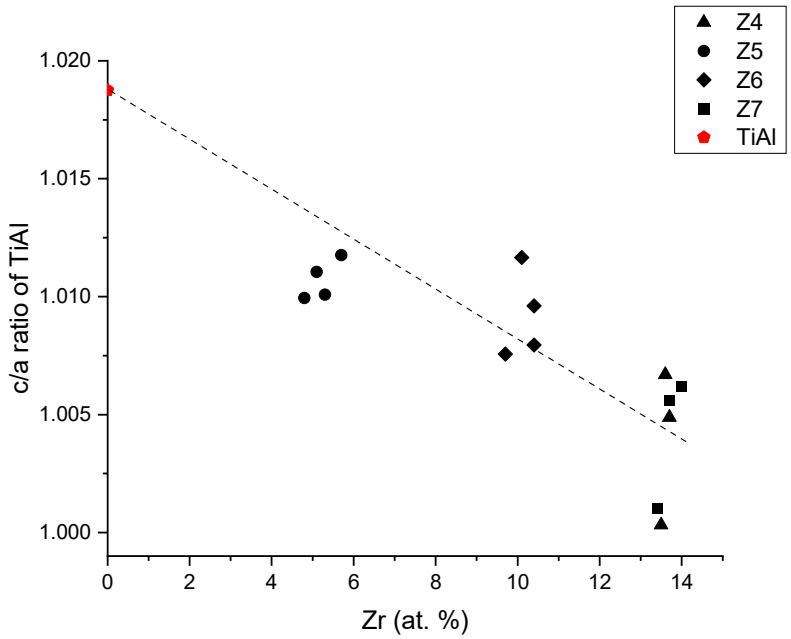

Figure 13. The c/a ratio of TiAl depending on the Zr content as determined by EPMA. Binary TiAl taken from [30].

4. Conclusions

The addition of Zr in TiAl-based alloys is beneficial in enhancing the creep resistance and increasing the strength of TiAl through solid solution hardening. Our recent assessment of the Ti—Al—Zr system as well as recent CALPHAD modellings showed the necessity for more experimental data of homogenized alloys. Therefore, four partial isothermal sections were experimentally established through SEM, EPMA, (HE)XRD, TEM, and DTA of six different alloy compositions heat treated at 1000–1300 °C.

It is now clear that B2-ordered β_0 already exists at 1000 °C and remains stable up to at least 1300 °C. Phase equilibria at all temperatures are different from the ones established before. While previous isothermal sections showed a large solid solubility of Ti in Zr_5Al_3, it is now clear that this phase is stabilized by impurities, most noteworthy oxygen. Therefore, much effort was spent to keep impurity levels as low as possible. By that, only traces of Zr_5Al_3 were observed, and phase equilibria between βTi,Zr/β_0, TiAl, and $ZrAl_2$ were determined at all temperatures. These results give a new understanding of phase equilibria in the Ti—Al—Zr system between 1000 and 1300 °C. This knowledge can now be used to set up the next generation of advanced CALPHAD databases, which help to develop TiAl-based alloys with improved properties.

Author Contributions: Z.K., Data curation, performing experimental investigations and conducting formal analyses, writing original draft, and visualization. B.R., TEM analyses, review, editing, and project administration. K.H., HE-XRD investigations and analyses, review and editing. M.P., Conceptualization, validation, writing—review and editing, supervision, project administration and funding acquisition. All authors have read and agreed to the published version of the manuscript.

Funding: This project has received funding from the Clean Sky 2 Joint Undertaking under the European Union's Horizon 2020 research and innovation programme under grant agreement no. 820647.

Data Availability Statement: Not applicable.

Acknowledgments: The authors would like to thank D. Klapproth and M. Kulse for alloy production, D. Kurz for wet chemical analysis, and I. Wossack and B. Breitbach for their help with performing EPMA and XRD analyses, respectively.

Conflicts of Interest: The authors declare no conflict of interest.

References

1. Bewlay, B.; Weimer, M.; Kelly, T.; Suzuki, A.; Subramanian, P. The science, technology, and implementation of TiAl alloys in commercial aircraft engines. *MRS Online Proc. Libr.* **2013**, *1516*, 49–58. [CrossRef]
2. Clemens, H.; Mayer, S. Design, processing, microstructure, properties, and applications of advanced intermetallic TiAl alloys. *Adv. Eng. Mater.* **2013**, *15*, 191–215. [CrossRef]
3. Clemens, H.; Smarsly, W.; Güther, V.; Mayer, S. Advanced intermetallic titanium aluminides. In Proceedings of the 13th World Conference on Titanium; John Wiley & Sons: Hoboken, NJ, USA, 2016; pp. 1189–1200.
4. Neumeier, S.; Bresler, J.; Zenk, C.; Haußmann, L.; Stark, A.; Pyczak, F.; Göken, M. Partitioning behavior of Nb, Ta, and Zr in fully lamellar $\gamma/\alpha 2$ titanium aluminides and its effect on the lattice misfit and creep behavior. *Adv. Eng. Mater.* **2021**, *23*, 2100156. [CrossRef]
5. Bresler, J.; Neumeier, S.; Ziener, M.; Pyczak, F.; Göken, M. The influence of niobium, tantalum and zirconium on the microstructure and creep strength of fully lamellar $\gamma/\alpha 2$ titanium aluminides. *Mater. Sci. Eng. A* **2019**, *744*, 46–53. [CrossRef]
6. Kainuma, R.; Fujita, Y.; Mitsui, H.; Ohnuma, I.; Ishida, K. Phase equilibria among α (hcp), β (bcc) and γ (L10) phases in Ti–Al base ternary alloys. *Intermetallics* **2000**, *8*, 855–867. [CrossRef]
7. Allen, M.; Güther, V.; Lindemann, J.; Kardos, S. Solid Solution Strengthening of TiAl Alloys with Zirconium. In Proceedings of the Intermetallics 2021, Bad Staffelstein, Germany, 4–8 October 2021; pp. 73–74.
8. Wimler, D.; Lindemann, J.; Reith, M.; Kirchner, A.; Allen, M.; Vargas, W.G.; Franke, M.; Klöden, B.; Weißgärber, T.; Güther, V. Designing advanced intermetallic titanium aluminide alloys for additive manufacturing. *Intermetallics* **2021**, *131*, 107109. [CrossRef]
9. Cheng, T.; Willis, M.; Jones, I. Effects of major alloying additions on the microstructure and mechanical properties of γ-TiAl. *Intermetallics* **1999**, *7*, 89–99. [CrossRef]
10. Sornadurai, D.; Panigrahi, B.; Sastry, V.S. Ramani, Crystal structure and X-ray powder diffraction pattern of Ti2ZrAI. *Powder Diffr.* **2000**, *15*, 189–190. [CrossRef]
11. Premkumar, M.; Prasad, K.S.; Singh, A.K. Structure and stability of the B2 phase in Ti–25Al–25Zr alloy. *Intermetallics* **2009**, *17*, 142–145. [CrossRef]
12. Muradyan, G.; Dolukhanyan, S.; Aleksanyan, A.; Ter-Galstyan, O.; Mnatsakanyan, N. Regularities and Mechanism of Formation of Aluminides in the TiH2-ZrH2-Al System. *Russ. J. Phys. Chem. B* **2019**, *13*, 86–95. [CrossRef]
13. Miyajima, Y.; Ishikawa, K.; Aoki, K. Hydrogen-induced amorphization in Ti–Al–Zr compounds with D019, B2 and FCC structures. *Mater. Trans.* **2002**, *43*, 1085–1088. [CrossRef]
14. Cheng, T.; Loretto, M. The decomposition of the beta phase in Ti–44Al–8Nb and Ti–44Al–4Nb–4Zr–0.2 Si alloys. *Acta Mater.* **1998**, *46*, 4801–4819. [CrossRef]
15. Ballor, J.; Li, T.; Prima, F.; Boehlert, C.J.; Devaraj, A. A review of the metastable omega phase in beta titanium alloys: The phase transformation mechanisms and its effect on mechanical properties. *Int. Mater. Rev.* **2022**, 1–20. [CrossRef]
16. Huang, Z. Ordered ω phases in a 4Zr–4Nb-containing TiAl-based alloy. *Acta Mater.* **2008**, *56*, 1689–1700. [CrossRef]
17. Jiang, H.; Hu, D.; Wu, X. Thermal stability of the omega phase in Zr-containing TiAl alloys. *J. Alloys Compd.* **2009**, *475*, 134–138. [CrossRef]
18. Huang, Z. Thermal stability of Ti–44Al–4Nb–4Zr–0.2 Si–1B alloy. *Intermetallics* **2013**, *42*, 170–179. [CrossRef]
19. Kattner, U.R. The Calphad method and its role in material and process development. *Tecnol. Metal. Mater. Min.* **2016**, *13*, 3. [CrossRef]
20. Kahrobaee, Z.; Palm, M. Critical Assessment of the Al-Ti-Zr System. *J. Phase Equilibria Diffus.* **2020**, *41*, 687–701. [CrossRef]
21. Deng, Z.; Zhao, D.; Huang, Y.; Chen, L.; Zou, H.; Jiang, Y.; Chang, K. Ab initio and CALPHAD-type thermodynamic investigation of the Ti-Al-Zr system. *J. Min. Metall. Sect. B* **2019**, *55*, 427–437. [CrossRef]
22. Wang, J.; Zheng, W.; Xu, G.; Zeng, X.; Cui, Y. Thermodynamic assessment of the Ti–Al–Zr system and atomic mobility of its bcc phase. *Calphad* **2020**, *70*, 101801. [CrossRef]
23. Lü, K.L.; Yang, F.; Xie, Z.Y.; Liu, H.S.; Cai, G.M.; Jin, Z.P. Isothermal section of Al−Ti−Zr ternary system at 1073 K. *Trans. Nonferrous Met. Soc. China* **2016**, *26*, 3052−3058. [CrossRef]
24. Yang, F.; Xiao, F.H.; Liu, S.G.; Dong, S.S.; Huang, L.H.; Chen, Q.; Cai, G.M.; Liu, H.S.; Jin, Z.P. Isothermal section of Al–Ti–Zr ternary system at 1273 K. *J. Alloys Compd.* **2014**, *585*, 325–330. [CrossRef]
25. Shirokova, N.I.; Nartova, T.T.; Kornilov, I.I. Исследование равновесия и свойств сплавов Ti-Zr-Al (Investigation of the phase equilibrium and properties of Ti-Zr-Al alloys). *Izv. Akad. Nauk. SSSR. Met.* **1968**, *1968*, 183–187.
26. Thermo-Calc Software AB, Next Generation TiAl Alloys Advanced by New European Consortium. Available online: https://thermocalc.com/blog/next-generation-tial-alloys-advanced-by-new-european-consortium/ (accessed on 28 March 2019).
27. Massalski, T.B. *Binary Alloy Phase Diagrams*, 2nd ed.; ASM International: Metals Park, OH, USA, 1990.
28. Schuster, J. Al-Zr binary phase diagram evaluation. In *MSI Eureka*; Effenberg, G., Ed.; Materials Science International Services GmbH (MSI): Stuttgart, Germany, 2004.
29. Blackburn, M.J. The ordering transformation in titanium: Aluminum alloys containing up to 25 at. pct Al. *Trans. Metall. Soc. AIME* **1967**, *239*, 1200–1208.
30. Braun, J.; Ellner, M.; Predel, B. Experimental investigation of the structure and stability of the phase TiAl. *Z. Metallkd.* **1995**, *86*, 870–876.

31. Kasahara, K.; Hashimoto, K.; Doi, H.; Tsujimoto, T. Crystal structure and hardness of TiAl phase containing zirconium. *Nippon. Kinzoku Gakkaishi J. Jpn. Inst. Met.* **1987**, *51*, 278–284.
32. Distl, B.; Dehm, G.; Stein, F. Effect of oxygen on high-temperature phase equilibria in ternary Ti-Al-Nb Alloys. *Z. Anorg. Allg. Chem.* **2020**, *646*, 1151–1156.
33. T'sai, L.S.; Hogness, T.R. The diffusion of gases through fused quartz. *J. Phys. Chem.* **2002**, *36*, 2595–2600. [CrossRef]
34. Kainuma, R.; Palm, M.; Inden, G. Solid-phase equilibria in the Ti-rich part of the Ti-Al system. *Intermetallics* **1994**, *2*, 321–332. [CrossRef]
35. *Powder Diffraction File PDF-2, Release 2004*; International Center for Diffraction Data: Newtown Square, PA, USA, 2004.
36. Giannuzzi, L.A.; Stevie, F.A. *Introduction to Focused Ion Beams Instrumentation, Theory, Techniques and Practice*; Springer: New York, NY, USA, 2005.
37. Mayer, J.; Giannuzzi, L.A.; Kamino, T.; Michael, J. TEM sample preparation and FIB-induced damage. *MRS Bull.* **2007**, *32*, 400–407. [CrossRef]
38. Schell, N.; King, A.; Beckmann, F.; Fischer, T.; Müller, M.; Schreyer, A. The high energy materials science beamline (HEMS) at PETRA III. In *Materials Science Forum*; Trans Tech Publications Ltd.: Bäch, Switzerland, 2014; pp. 57–61.
39. Schell, N. Synchrotron-Based Capabilities for Studying Engineering Materials at PETRA-III. *Synchrotron Radiat. News* **2017**, *30*, 29–34. [CrossRef]
40. Hammersley, A. FIT2D: A multi-purpose data reduction, analysis and visualization program. *J. Appl. Crystallogr.* **2016**, *49*, 646–652. [CrossRef]
41. Malfliet, A.; Kozlov, A.; Lebrun, N. Ti-Zr binary phase diagram evaluation. In *MSI Eureka*; Effenberg, G., Ed.; Materials Science International services GmbH (MSI): Stuttgart, Germany, 2015; pp. 1–12.
42. Palm, M. Al-Ti binary phase diagram evaluation. In *MSI Eureka*; Effenberg, G., Ed.; Materials Science International services GmbH (MSI): Stuttgart, Germany, 2020.
43. Schuster, J.C.; Palm, M. Reassessment of the binary Aluminium-Titanium phase diagram. *J. Phase Equilibria Diffus.* **2006**, *27*, 255–277. [CrossRef]
44. Kim, S.-J.; Kematick, R.; Yi, S.; Franzen, H. On the stabilization of Zr5Al3 in the Mn5Si3-type structure by interstitial oxygen. *J. Less Common Met.* **1988**, *137*, 55–59. [CrossRef]
45. Kwon, Y.U.; Rzeznik, M.A.; Guloy, A.; Corbett, J.D. Impurity stabilization of phases with the manganese silicide (Mn5Si3)-type structure: Questions regarding lanthanum-tin (La5Sn3) and zirconium silicide (Zr5Si3). *Chem. Mater.* **1990**, *2*, 546–550. [CrossRef]
46. Stein, F.; Sauthoff, G.; Palm, M. Phases and phase equilibria in the Fe-Al-Zr system. *Z. Metallkd.* **2004**, *96*, 469–485. [CrossRef]
47. Tanda, D.; Tanabe, T.; Tamura, R.; Takeuchi, S. Synthesis of ternary L10 compounds of Ti–Al–Zr system and their mechanical properties. *Mat. Sci. Eng. A* **2004**, *387–389*, 991–995. [CrossRef]
48. Banerjee, S.; Mukhopadhyay, P. *Phase Transformations: Examples from Titanium and Zirconium Alloys*; Elsevier: Oxford, UK, 2010.
49. Mayer, S.; Petersmann, M.; Fischer, F.D.; Clemens, H.; Waitz, T.; Antretter, T. Experimental and theoretical evidence of displacive martensite in an intermetallic Mo-containing γ-TiAl based alloy. *Acta Mater.* **2016**, *115*, 242–249. [CrossRef]
50. Nartova, T.T.; Shirokova, N.I. Phase equilibria and heat resistance of Ti-Zr-Al alloys. *Izv. Akad. Nauk. SSSR. Met.* **1970**, *1970*, 194–198.
51. Shirokova, N.I.; Nartova, T.T. Investigation of the phase equilibrium and properties of alloys of the titanium corner of the system Ti-Zr-Al. In *Titanovyye Splavy dlya Novoy Tekhniki*; Sazhin, N.P., Ed.; Nauka: Moscow, 1968; pp. 101–106.
52. Kornilov, I.I.; Boriskina, N.G. Study of the phase structure of the alloys of the system Ti-Al-Zr along the Ti3Al-Zr section. In *Metallovedeniye Titana*; Kornilov, I.I., Ed.; Nauka: Moscow, 1964; pp. 58–66.
53. Pylaeva, Y.N.; Volkova, M.A. Study of the alloys of the ternary system Ti-Al-Zr. In *Metallovedeniye Titana*; Kornilov, I.I., Ed.; Nauka: Moscow, 1964; pp. 38–42.
54. Kornilov, I.I.; Nartova, T.T.; Savel'yeva, M.M. Phase equilibrium of alloys of the section Ti3Al-Zr of the ternary system Ti-Al-Zr. In *Metallovedeniye Titana*; Kornilov, I.I., Ed.; Nauka: Moscow, Russia, 1964; pp. 53–57.
55. Sandlin, D.R.; Klung, H.A. *A Phase Study of a Selected Portion of the Ti-Al-Zr Ternary System including Lattice Parameter Determination for the Ti-Al Gamma Phase*; School of Engineering, Air Force Institute of Technology, Air University, Wright-Patterson Airforce Base: Fairborn, OH, USA, 1961.
56. Troup, D.H. *An Investigation of the Gamma Phase of the Binary Titanium-Aluminum Alloy with Zirconium Additions*; School of Engineering, Air Force Institute of Technology, Air University, Wright-Patterson Airforce Base: Fairborn, OH, USA, 1962; pp. 1–89.
57. Jiang, X.; Zhou, Y.; Feng, Z.; Xia, C.; Tan, C.; Liang, S.; Zhang, X.; Ma, M.; Liu, R. Influence of Zr content on β-phase stability in α-type Ti–Al alloys. *Mater. Sci. Eng. A* **2015**, *639*, 407–411. [CrossRef]
58. Fan, F.; Gu, Y.; Xu, G.; Chang, H.; Cui, Y. Diffusion Research in BCC Ti-Al-Zr Ternary Alloys. *J. Phase Equilibria Diffus.* **2019**, *40*, 686–696. [CrossRef]
59. Spragins, S.; Myers, J.; Saxer, R. Influence of Zirconium Additions on the Epsilon Phase of the Titanium-Aluminium System. *Nature* **1965**, *207*, 183–184. [CrossRef]
60. Abreu, D.; Silva, A.; Santos, J.; Barros, D.; Barros, C.; Chaia, N.; Nunes, C.; Coelho, G. Liquidus projection of the Al–Ti–Zr system. *J. Alloys Compd.* **2020**, *849*, 156463. [CrossRef]

61. Davies, F.C. The Effects of Ternary Additions on Lattice Parameters in the Gamma Phase of Titanium-Aluminum Alloy System. PhD Thesis, School of Engineering, Air Force Institute of Technology, Air University, Wright-Patterson Airforce Base, Fairborn, OH, USA, 1959. cited in (1962 Tro).
62. Hashimoto, K.; Doi, H.; Kasahara, K.; Tsujimoto, T.; Suzuki, T. Effects of third elements on the structures of TiAl-based alloys. *Nippon. Kinzoku Gakkaishi J. Jpn. Inst. Met.* **1988**, *52*, 816–825. [CrossRef]
63. Kawabata, T.; Fukai, H.; Izumi, O. Effect of ternary additions on mechanical properties of TiAl. *Acta Mater.* **1998**, *46*, 2185–2194. [CrossRef]